Two-Color Strong-Field Photoelectron Spectroscopy and the Phase of the Phase

S. Skruszewicz, J. Tiggesbäumker, K.-H. Meiwes-Broer, M. Arbeiter, Th. Fennel, and D. Bauer
Institut für Physik, Universität Rostock, 18051 Rostock, Germany
(Received 2 February 2015; published 22 July 2015)

The presence of a weak second-harmonic field in an intense-laser ionization experiment affects the momentum-resolved electron yield, depending on the relative phase between the ω and the 2ω component. The proposed two-color "phase-of-the-phase spectroscopy" quantifies for each final electron momentum a relative-phase contrast (RPC) and a phase of the phase (PP) describing how much and with which phase lag, respectively, the yield changes as a function of the relative phase. Experimental results for RPC and PP spectra for rare gas atoms and CO_2 are presented. The spectra demonstrate a rather universal structure that is analyzed with the help of a simple model based on electron trajectories, wave-packet spreading, and (multiple) rescattering. Details in the PP and RPC spectra are target sensitive and, thus, may be used to extract structural (or even dynamical) information with high accuracy.

DOI: 10.1103/PhysRevLett.115.043001 PACS numbers: 32.80.Rm, 33.60.+q, 34.80.Qb

Momentum-resolved photoelectron spectra from strong-field ionization of atoms and molecules contain a wealth of information about the ionizing laser field, the target, and ultrafast processes that may occur in it (see, e.g., Refs. [1,2] for recent overviews). If one is able to disentangle this information, one may use photoelectron spectra to image the entire ionization dynamics and the structural information convoluted into it. Thanks to the appealing possibility to analyze most of the strong-field ionization dynamics in terms of semiclassical electron trajectories, it has been demonstrated that many of the complex and, at first sight, puzzling features could finally be explained in simple and intuitive terms. Examples are various low-energy structures [3–10], intra- and intercycle interferences [11–13], "holographic side lobes" and the role of multiple returns [14–16], molecular strong-field ionization [17,18], or "interference carpets" [19].

Refined strong-field experiments make use of additional experimental "knobs," such as a pump-probe delay, a carrier-envelope phase (CEP) in the case of few-cycle pulses (see, e.g., Refs. [20–22] for reviews), or a relative phase between two laser fields of different frequency [23–29]. The resulting changes in the photoelectron or complementary high-harmonics spectra may then help to unequivocally identify certain ionization scenarios. In this Letter, we present experimental results obtained with a colinear, two-color laser setup.

Consider the measurement of an observable (here the electron yield). If this observable depends on a tunable parameter (here the relative phase between the ω and the 2ω pulse), a measurement of the change of the observable as a function of the parameter reveals additional information about the underlying physical mechanism (here the target and laser-sensitive ionization dynamics). A general question is how to represent this additional information. If the parameter is periodic (like the relative phase), a Fourier transform of the observable seems adequate. In our case, the momentum-resolved photoemission signal is Fourier transformed with respect to the relative phase. The absolute value of the complex Fourier transform gives a relative-phase contrast (RPC), its phase the "phase of the phase" (PP). In this Letter, we present experimental RPC and PP spectra for various targets and analyze their common features in terms of "simple man's theory" (SMT). The main findings are (i) the overall structure of the PP spectra is largely target independent and displays features that can be assigned to certain electron trajectories; (ii) target-dependent features are clearly visible in the RPC and PP spectra, thus, making two-color PP spectroscopy an attractive approach for revealing structural information.

The basic structure of "ordinary" photoelectron spectra is qualitatively well understood. For linear laser polarization, the so-called "direct electrons" extend up to energies $p_z^2/2 = A_0^2/2 = 2U_p$, where p_z is the photoelectron momentum along the polarization direction, A_0 is the vector potential amplitude, and $U_p = A_0^2/4$ is the ponderomotive energy (atomic units are used unless otherwise stated). If electrons are driven back to their parent ion by the laser field, energies up to $10U_p$ may occur upon rescattering. A wealth of information is encoded in this high-energy above-threshold ionization part of the photoelectron spectra about both (i) the driving laser field and (ii) the structure of the target [30,31] (via its scattering cross section [32,33]). Moreover, high-energy above-threshold ionization is more robustly accessible to theoretical modeling than the low-energy part of photoelectron spectra, which is plagued by the necessity to take Coulomb corrections into account [34–39].

Bichromatic $\omega - 2\omega$ pulses with parallel polarizations of the field components and adjustable relative phase φ were generated with a setup similar to the one in Ref. [40]. Briefly, a Ti:sapphire laser system provides 100-fs pulses

at 794 nm. The second harmonic is generated in a 100-μm-thick BBO I crystal. The $\omega - 2\omega$ intensity ratio is controlled by detuning the phase matching conditions through a tilt of the crystal. Birefringent calcite crystals compensate for the time lag between the ω and 2ω pulse. The relative-phase lag is controlled by two glass wedges mounted on piezo-driven motors. The laser pulses are focused into the extraction region of a homebuilt high-energy velocity-map-imaging (VMI) spectrometer [41] by a concave silver mirror having a focal length of 300 mm. Photoemission from Xe was used to optimize the pulse overlap. The MCP backplate of the detector system is gated using a fast electronic switch to suppress spurious signals.

Our two-color field is described by the vector potential

$$\boldsymbol{A}(t) = A_0 \boldsymbol{e}_z [\sin \omega t + \xi \sin(2\omega t + \varphi)] \qquad (1)$$

in dipole approximation. The use of long pulses ensures that envelope effects are unimportant. Throughout this work, the 2ω field is kept weak ($\xi \ll 1$).

Figure 1 introduces schematically the two quantities—RPC P and PP Φ—used to describe how the photoelectron yield $Y(\varphi)$ changes as a function of the relative phase. For each final momentum p_z, p_x, the fundamental change in the yield, i.e., $Y_1(\varphi) = P\cos(\varphi + \Phi)$, is extracted via the Fourier analysis mentioned above. The fundamental ($N = 1$) component is found to dominate over higher-harmonic contributions Y_N, $N > 1$ for most final momenta. A similar analysis has been performed previously with respect to the CEP for SiO_2 nanospheres [42].

Experimentally determined RPC and PP spectra for Ar are presented in Fig. 2. The RPC in Fig. 2(a) shows that the direct electrons vary most with φ (black and dark gray), while the rescattered electrons vary with about 1 order of magnitude less contrast. The direct electrons with $p_z > 0$ in the PP spectrum in Fig. 2(b) behave predominantly $\sin\varphi$ to $-\cos\varphi$-like (blue to black area labeled 1), the ones with $p_z < 0$ behave $\cos\varphi$ to $-\sin\varphi$-like (green to red, 2). Most of the rescattered electrons behave phasewise similar to the direct electrons in the *opposite* direction (3 red to black, and 4 blue to green). However, in the semicircle-shaped momentum regions, 5 and 6 beyond the respective $2U_p$ cutoffs, the electrons continue to follow phasewise the direct electrons in the *same* direction, i.e., 2 and 1, respectively. This effect will be discussed in more detail below. Note that the overall absolute phase is not determined by the experiment so that a cyclic shift of the color code for the experimental PP spectra is permissible.

In Fig. 3 we show RPC and PP spectra for Kr, Xe, and randomly aligned CO_2. Figures 2(b), 3(b), 3(d), and 3(f) show that the overall structure of the PP spectra is universal: they resemble two overlapping clubs [indicated in Fig. 3(f)], one colored in red to green [regions 2, 5, and 4 in Fig. 2(b)], and the other one blue to black (1, 6, and 3). The blunt parts of the clubs (regions 3 and 4) represent rescattered electrons. The tip regions 5 and 6 are investigated below. While the overall structure is similar for all species, a target dependence is most obvious in the RPC spectra Figs. 3(a), 3(c), 3(e), and 2(a) and also reflected in detailed features of the PP spectra. This allows two-color spectroscopy to be employed for imaging and as a sensitive test of theoretical models. In what follows, we aim to reproduce the results of Fig. 2 via simple modeling using SMT.

SMT (see, e.g., Refs. [22,43,44]) should be able to reveal the origins of the common overall features observed in the PP spectra. Given a vector potential (1) the electron

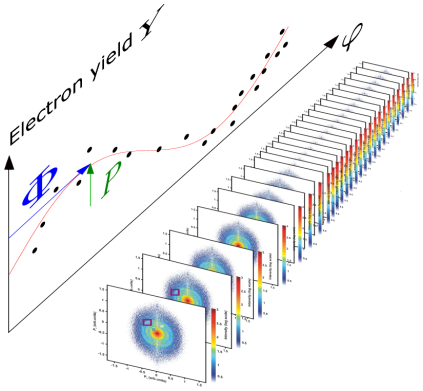

FIG. 1 (color online). Schematic illustration of RPC P and PP Φ. Given a sequence of photoelectron momentum distributions (as obtained with the VMI spectrometer) for varied relative phase φ, the change in electron yield (dots) for given photoelectron momentum (small square in the spectra) is fitted by $P\cos(\varphi + \Phi)$ (red curve).

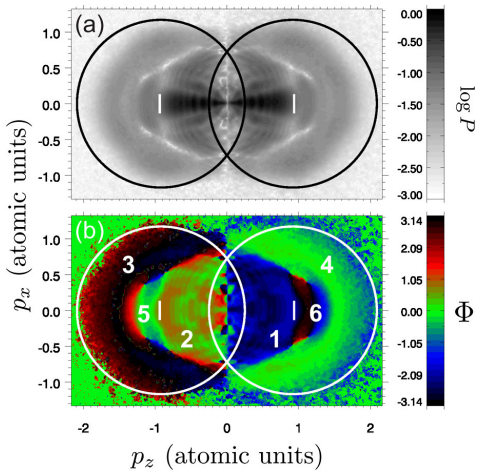

FIG. 2 (color online). Experimental RPC (a) and PP (b) spectra for Ar, calculated from 66 Abel-projected VMI spectra per φ interval $[0, 2\pi]$. The 794- and 397-nm components of the 100-fs two-color pulse had intensities $\simeq 10^{14}$ and 10^{12} W/cm^2, respectively (i.e., $\xi = 0.05$). In (a), P has been normalized to max P. Circles and vertical lines indicate $10U_p$ rescattering rings and $2U_p$ cutoffs, respectively. White numbers in (b) are referred to in text.

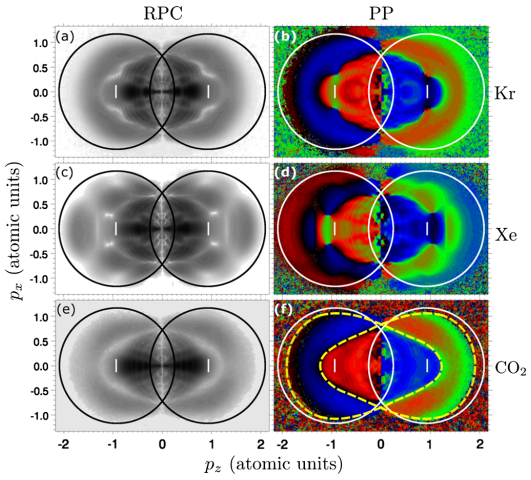

FIG. 3 (color online). Experimental RPCs (left) and PPs (right) for Kr (top), Xe (middle), and randomly aligned CO_2 (bottom). Laser intensities and color coding as in Fig. 2. The yellow dashed lines in (f) indicate the "clubs" discussed in the text.

momentum before rescattering reads $\boldsymbol{p}(\tau)/A_0 = \bar{p}(\tau)\boldsymbol{e}_z = \boldsymbol{a}(\tau) - \boldsymbol{a}(\tau_1)$. The dimensionless time $\tau = \omega t$, momentum $\bar{p} = p/A_0$, and vector potential $\boldsymbol{a} = \boldsymbol{A}/A_0$ are introduced to highlight the universal scaling of SMT, and $\tau_1 = \omega t_1$ with t_1 the ionization time. Assuming isotropic scattering and considering the planar motion in, e.g., the x-z plane, the momentum after rescattering and once the pulse is off reads

$$\begin{pmatrix} \bar{p}_z \\ \bar{p}_x \end{pmatrix} = \begin{pmatrix} -a(\tau_2) \\ 0 \end{pmatrix} + [a(\tau_2) - a(\tau_1)] \begin{pmatrix} \cos\theta \\ \sin\theta \end{pmatrix}. \quad (2)$$

Here, $\tau_2 = \omega t_2 > \tau_1$ with t_2 the rescattering time and θ the scattering angle. The maximum momentum $\bar{p}_{\max} = \sqrt{5}$ corresponds to the well-known cutoff energy $10U_p$, which occurs if ionization happens at $\tau_1/2\pi = 0.543$ (or at 0.043 in the opposite direction) and the $\theta = \pi$ backscattering at $\tau_2/2\pi = 1.22$ (0.72). The $10U_p$ rescattering rings, i.e., rings in the momentum plane centered at $-a(\tau_2)\boldsymbol{e}_z$ with radius $|a(\tau_2) - a(\tau_1)|$, are shown in Fig. 4(a) below and indicated in all experimental spectra and those calculated via the numerical solution of the time-dependent Schrödinger equation (TDSE). If electrons do not scatter during the first but the second return, they end up in the opposite z direction and generate second-return rescattering rings. In particular, if ionization and rescattering occur at $\tau_1/2\pi = 0.519$ (0.019) and $\tau_2/2\pi = 1.74$ (1.24), respectively, a local maximum cutoff energy of $7U_p$ is reached, also indicated in Fig. 4(a) [respective trajectory shown in Fig. 4(b)].

The fundamental club structure of the PP spectra is easy to reproduce within SMT: (i) looping over τ_1 and $\tau_2 > \tau_1$ all electron trajectories that actually rescatter are considered, and (ii) weighted by $W = W_r W_i$ where W_i is an ionization and W_r a rescattering probability. An instantaneous tunneling rate through a triangular barrier [45]

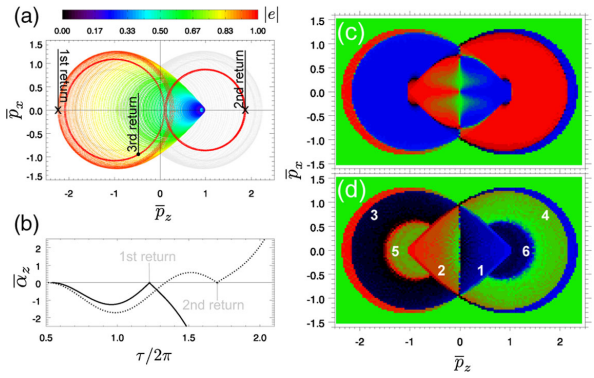

FIG. 4 (color online). (a) Final SMT photoelectron momenta for $\xi = 0$, absolute value of electric field at ionization time $|\boldsymbol{e}(\tau_1)|$ color coded. Rings representing local maxima in final momentum $|\bar{p}_z|$ due to rescattering during the first, second, and third return are labeled. For better visibility, final momenta in respective opposite directions (originating from electrons emitted half a laser cycle earlier) are plotted in light gray. (b) Normalized excursion $\bar{\alpha}_z$ of electron rescattering at first (solid) and second return (dotted), respectively, leading to final momenta indicated as x in (a). SMT PP spectra for $\xi = 0.05$, taking into account (c) ionization and wave-packet spreading ($s = 3/2$) and (d) additionally a scattering cross section (3) (with $Z = 18$ and $\mu = 1/2$). Same color coding in (c) and (d) as in previous figures. White numbers in (d) analogous to Fig. 2(b).

$W_i(\tau_1) \sim \exp[-2/3|\boldsymbol{e}(\tau_1)|]$ [with $\boldsymbol{e}(\tau) = -\partial_\tau \boldsymbol{a}(\tau)$ the dimensionless electric field] has been taken. We are not interested in absolute numbers here, as our SMT modeling should be robust and depend only on $\boldsymbol{a}$ and τ. In a first crude approximation, $W_r(\tau_2 - \tau_1) = (\tau_2 - \tau_1)^{-s}$ with a spreading exponent $s > 0$ has been chosen. Such a rescattering probability accounts for wave-packet spreading (see, e.g., Refs. [22,43]) but neglects any momentum and angular dependence of the scattering cross section. If several trajectories end up in the same final momentum bin, only the most probable has been considered, thus, neglecting interference effects. The direct electrons have been weighted by $W_i^{(\mathrm{dir})}(\tau_1) = W_i(\tau_1)\exp(-\beta\bar{p}_x^2/|\boldsymbol{e}(\tau_1)|)$ with $\beta = 15$ (to produce a reasonable lateral spread of the momentum distribution). The result of such a simple modeling for $s = 3/2$ is shown in Fig. 4(c). The spreading exponent has been chosen smaller than $s = 3$ for free 3D Gaussian wave-packet spreading in order to mimic Coulomb focusing [46]. The structure of the two overlapping clubs—one red, the other blue—is clearly visible. The weak ($\xi = 0.05$) 2ω component leads to a small extension of the rescattering cutoff (small strip of opposite color around the blunt club ends).

Obvious disagreements between Fig. 4(c) and all experimental results are the oversimplified behavior consisting of essentially only two PPs (red or blue) and the too-short low-momentum tip of the club ending at $|\bar{p}_z| = 1$ corresponding to the $2U_p$ cutoff for direct electrons. In all experimental and TDSE results, the club tips extend beyond $2U_p$ [see

regions 5 and 6 in Fig. 2(b)]. In order to reveal the origin of this mismatch, we first note that in the SMT modeling of Fig. 4(c), the trajectories that rescatter at their first return dominate because of the $(\tau_2 - \tau_1)^{-s}$ penalty for later returns. This is the reason why there is essentially only a sin like or a $-$ sin like behavior for all final momenta (i.e., blue or red). In a refined modeling, a rescattering probability $\sim W_r(\tau_2 - \tau_1)\sigma(q, \theta)$ with a differential scattering cross section (in first Born approximation) of the form

$$\sigma(q,\theta) = \frac{(2Z)^2}{[\mu^2 + 4q^2\sin^2(\theta/2)]^2}, \qquad q = a(\tau_2) - a(\tau_1) \tag{3}$$

for a screened potential $V(r) = -Z\exp(-\mu r)/r$ has been employed. The resulting spectrum in Fig. 4(d) is in much better agreement with the experiments. In fact, given the simple modeling, the agreement is striking. Going from Fig. 4(c) to 4(d), the PP in regions 3 and 4 changes from sin (blue) to $-$ cos like (black) for $\bar{p}_z < 0$ and from $-$ sin (red) to cos like (green) for $\bar{p}_z > 0$. The reason for this change lies in the introduction of an additional functional dependence on the relative phase via the cross section $\sigma(q(\varphi), \theta)$.

Because in the SMT all spectral features can be understood in terms of electron trajectories, we were able to identify the origin of the ringlike extensions 5 and 6 beyond $2U_p$. Figure 4(a) suggests that these features are due to electrons that rescatter during the second return because the corresponding rescattering rings are centered around the $2U_p$ cutoffs. A cross section of the form (3) favors forward scattering (i.e., small θ), and the more so, the larger the instantaneous scattering momentum $q = |a(\tau_2) - a(\tau_1)|$ is. As a consequence, the trajectories which scatter with lower momentum later during the second return (incident from the opposite direction) may have a higher probability for large θ than the trajectories that rescatter during the first return, despite the wave-packet-spreading penalty for late returns. It is, thus, the competition between the probability factors governing wave-packet spreading and the momentum-dependent large-angle scattering which is responsible for the club tips beyond $2U_p$.

Figure 5 shows RPC and PP spectra for Ar from a TDSE simulation [47] in single-active electron approximation. Abel-projected photoelectron momentum spectra were calculated for different φ and subsequently treated like the experimental spectra. The correct ionization potential of Ar was imposed by choosing the $3p_0$ orbital in the effective potential $V(r) = -[1 + 17\exp(-2.11375r)]/r$ as the initial state. Comparison with Fig. 2 yields satisfactory agreement with respect to the overall club structure in the PP and the qualitative features in the RPC spectra. We note that the dynamic range of the experimental detection is 2 orders of magnitude lower than the one shown for the TDSE. This might be the reason why the marked features close to the second-return cutoff in the TDSE PP spectrum

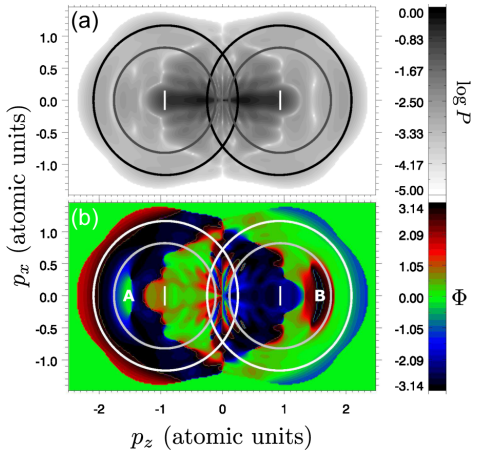

FIG. 5 (color online). RPC (a) and PP (b) spectra for Ar from TDSE (10^{14} W/cm^2, $\xi = 0.05$). Durations of sin^2-shaped pulses for 794 and 397 nm were 60 and 50 fs, respectively. Additionally to $2U_p$ cutoffs and $10U_p$ rings, second-return cutoff rings are included, which form boundaries for features labeled A and B. Slight left-right asymmetries visible in (a) are remnants of CEP dependence.

(labeled A and B) are absent in the experiment. The remaining differences could be due to the idealized pulses and the neglect of focal averaging in the simulation, slightly different laser parameters in experiment and simulation, or the possibly inadequate (but computationally unavoidable) assumption of a single-active electron in the TDSE calculations. In any case, such differences show the sensitivity of PP spectroscopy and its power to discriminate between various effects.

In summary, we have introduced systematic two-color spectroscopy based on RPC and PP spectra. The presence of the 2ω-field component tags each emission time according to how ionization probability changes as a function of the relative phase. This change is subsequently mapped through the actual electron dynamics to the final photoelectron momentum. Since several trajectories end up with the same final momentum, the trajectory with the largest change in general dominates. We have revealed and explained the universal overall structure of the PP spectra for various rare gas atoms and CO_2. We further have shown that details in both the RPC and the PP are target dependent, paving the way to employ them for imaging electronic structure or dynamics and as tests for theoretical predictions or cross sections. We also anticipate that two-color spectroscopy will be able to discriminate among coherent, delayed, or thermal electron emission, e.g., in nonsequential ionization of multielectron systems, because the relative-phase dependence is maintained, affected, or destroyed, respectively. Any spectral feature identified in an "ordinary" photoelectron spectrum and hypothetically attributed to a certain phenomenon (such as rescattering or focusing of certain trajectories, polarization of the target, or internal dynamics) can be further scrutinized, in that way

testing whether the PP and RPC signatures of this feature are in accordance with the predictions from the conjectured theory.

We thank M. Kling and S. Zherebtsov for bringing us in touch with the $\omega - 2\omega$ method and helpful support in the early stage of our studies. Fruitful discussions with M. Ivanov, computer time provided by the North-German Supercomputing Alliance (HLRN, Project No. mvp00004), and support through the Sonderforschungsbereich 652 of the German Science Foundation (DFG) are gratefully acknowledged.

[1] *Attosecond and XUV Physics, Ultrafast Dynamics and Spectroscopy*, edited by Th. Schultz and M. Vrakking (Wiley-VCH, Weinheim, 2014).
[2] *Progress in Ultrafast Intense Laser Science IX*, edited by K. Yamanouchi and K. Midorikawa (Springer, Heidelberg, 2013).
[3] C. I. Blaga, F. Catoire, P. Colosimo, G. G. Paulus, H. G. Muller, P. Agostini, and L. F. DiMauro, Nat. Phys. **5**, 335 (2009).
[4] W. Quan, Z. Lin, M. Wu, H. Kang, H. Liu, X. Liu, J. Chen, J. Liu, X. T. He, S. G. Chen, H. Xiong, L. Guo, H. Xu, Y. Fu, Y. Cheng, and Z. Z. Xu, Phys. Rev. Lett. **103**, 093001 (2009).
[5] C. Liu and K. Z. Hatsagortsyan, Phys. Rev. Lett. **105**, 113003 (2010).
[6] T.-M. Yan, S. V. Popruzhenko, M. J. J. Vrakking, and D. Bauer, Phys. Rev. Lett. **105**, 253002 (2010).
[7] A. Kästner, U. Saalmann, and J. M. Rost, Phys. Rev. Lett. **108**, 033201 (2012).
[8] Ch. Lemell, K. I. Dimitriou, X.-M. Tong, S. Nagele, D. V. Kartashov, J. Burgdörfer, and S. Gräfe, Phys. Rev. A **85**, 011403(R) (2012); Ch. Lemell, J. Burgdörfer, S. Gräfe, K. I. Dimitriou, D. G. Arbó, and X.-M. Tong, Phys. Rev. A **87**, 013421 (2013).
[9] J. Dura, N. Camus, A. Thai, A. Britz, M. Hemmer, M. Baudisch, A. Senftleben, C. D. Schröter, J. Ullrich, R. Moshammer, and J. Biegert, Sci. Rep. **3**, 2675 (2013).
[10] M. Möller, F. Meyer, A. M. Sayler, G. G. Paulus, M. F. Kling, B. E. Schmidt, W. Becker, and D. B. Milošević, Phys. Rev. A **90**, 023412 (2014).
[11] D. G. Arbó, K. L. Ishikawa, K. Schiessl, E. Persson, and J. Burgdörfer, Phys. Rev. A **81**, 021403(R) (2010).
[12] X.-B. Bian, Y. Huismans, O. Smirnova, K.-J. Yuan, M. J. J. Vrakking, and A. D. Bandrauk, Phys. Rev. A **84**, 043420 (2011).
[13] X.-M. Tong, P. Ranitovic, D. D. Hickstein, M. M. Murnane, H. C. Kapteyn, and N. Toshima, Phys. Rev. A **88**, 013410 (2013).
[14] Y. Huismans *et al.*, Science **331**, 61 (2011).
[15] Y. Huismans, A. Gijsbertsen, A. S. Smolkowska, J. H. Jungmann, A. Rouzée, P. S. W. M. Logman, F. Lépine, C. Cauchy, S. Zamith, T. Marchenko, J. M. Bakker, G. Berden, B. Redlich, A. F. G. van der Meer, M. Yu. Ivanov, T.-M. Yan, D. Bauer, O. Smirnova, and M. J. J. Vrakking, Phys. Rev. Lett. **109**, 013002 (2012).
[16] D. D. Hickstein, P. Ranitovic, S. Witte, X.-M. Tong, Y. Huismans, P. Arpin, X. Zhou, K. E. Keister, C. W. Hogle, B. Zhang, Ch. Ding, P. Johnsson, N. Toshima, M. J. J. Vrakking, M. M. Murnane, and H. C. Kapteyn, Phys. Rev. Lett. **109**, 073004 (2012).
[17] M. Meckel, D. Comtois, D. Zeidler, A. Staudte, D. Pavičić, H. C. Bandulet, H. Pépin, J. C. Kieffer, R. Dörner, D. M. Villeneuve, and P. B. Corkum, Science **320**, 1478 (2008).
[18] M. Odenweller, N. Takemoto, A. Vredenborg, K. Cole, K. Pahl, J. Titze, L. Ph. H. Schmidt, T. Jahnke, R. Dörner, and A. Becker, Phys. Rev. Lett. **107**, 143004 (2011).
[19] Ph. A. Korneev, S. V. Popruzhenko, S. P. Goreslavski, T.-M. Yan, D. Bauer, W. Becker, M. Kübel, M. F. Kling, C. Rödel, M. Wünsche, and G. G. Paulus, Phys. Rev. Lett. **108**, 223601 (2012).
[20] G. G. Paulus, F. Lindner, H. Walther, A. Baltuška, E. Goulielmakis, M. Lezius, and F. Krausz, Phys. Rev. Lett. **91**, 253004 (2003).
[21] F. Krausz and M. Ivanov, Rev. Mod. Phys. **81**, 163 (2009).
[22] D. B. Milošević, G. G. Paulus, D. Bauer, and W. Becker, J. Phys. B **39**, R203 (2006).
[23] J. Mauritsson, J. M. Dahlström, E. Mansten, and T. Fordell, J. Phys. B **42**, 134003 (2009).
[24] J. M. Dahlström, A. L'Huillier, and J. Mauritsson, J. Phys. B **44**, 095602 (2011).
[25] D. Ray, Z. Chen, S. De, W. Cao, I. V. Litvinyuk, A. T. Le, C. D. Lin, M. F. Kling, and C. L. Cocke, Phys. Rev. A **83**, 013410 (2011).
[26] D. Shafir, H. Soifer, B. D. Bruner, M. Dagan, Y. Mairesse, S. Patchkovskii, M. Yu. Ivanov, O. Smirnova, and N. Dudovich, Nature (London) **485**, 343 (2012).
[27] X. Xie, S. Roither, S. Gräfe, D. Kartashov, E. Persson, Ch. Lemell, Li Zhang, M. S. Schöffler, A. Baltuška, J. Burgdörfer, and M. Kitzler, New J. Phys. **15**, 043050 (2013).
[28] D. G. Arbó, S. Nagele, X.-M. Tong, X. Xie, M. Kitzler, and J. Burgdörfer, Phys. Rev. A **89**, 043414 (2014).
[29] M. Richter, M. Kunitski, M. Schöffler, T. Jahnke, L. P. H. Schmidt, Min Li, Y. Liu, and R. Dörner, Phys. Rev. Lett. **114**, 143001 (2015).
[30] M. Spanner, O. Smirnova, P. B. Corkum, and M. Yu. Ivanov, J. Phys. B **37**, L243 (2004).
[31] C. I. Blaga, J. Xu, A. D. DiChiara, E. Sistrunk, K. Zhang, P. Agostini, T. A. Miller, L. F. DiMauro, and C. D. Lin, Nature (London) **483**, 194 (2012).
[32] T. Morishita, Anh-Thu Le, Z. Chen, and C. D. Lin, Phys. Rev. Lett. **100**, 013903 (2008).
[33] Z. Chen, J. Phys. B **44**, 245601 (2011).
[34] S. V. Popruzhenko and D. Bauer, J. Mod. Opt. **55**, 2573 (2008).
[35] S. V. Popruzhenko, G. G. Paulus, and D. Bauer, Phys. Rev. A **77**, 053409 (2008).
[36] O. Smirnova, M. Spanner, and M. Ivanov, Phys. Rev. A **77**, 033407 (2008).
[37] L. Torlina and O. Smirnova, Phys. Rev. A **86**, 043408 (2012); L. Torlina, J. Kaushal, and O. Smirnova, Phys. Rev. A **88**, 053403 (2013).
[38] M. S. Gravielle, D. G. Arbò, J. E. Miraglia, and M. F. Ciappina, J. Phys. B **45**, 015601 (2012).

[39] T.-M. Yan and D. Bauer, Phys. Rev. A **86**, 053403 (2012).

[40] N. Dudovich, O. Smirnova, J. Levesque, Y. Mairesse, M. Yu. Ivanov, D. M. Villeneuve, and P. B. Corkum, Nat. Phys. **2**, 781 (2006).

[41] S. Skruszewicz, J. Passig, A. Przystawik, N. X. Truong, M. Köther, J. Tiggesbäumker, and K.-H. Meiwes-Broer, Int. J. Mass Spectrom. **365–366**, 338 (2014).

[42] S. Zherebtsov, F. Süßmann, C. Peltz, J. Plenge, K. J. Betsch, I. Znakovskaya, A. S. Alnaser, N. G. Johnson, M. Kübel, A. Horn, V. Mondes, C. Graf, S. A. Trushin, A. Azzeer, M. J. J. Vrakking, G. G. Paulus, F. Krausz, E. Rühl, T. Fennel, and M. F. Kling, New J. Phys. **14**, 075010 (2012).

[43] W. Becker, F. Grasbon, R. Kopold, D. B. Milošević, G. G. Paulus, and H. Walther, Adv. At. Mol. Opt. Phys. **48**, 35 (2002).

[44] P. Salières, B. Carré, L. Le Déroff, F. Grasbon, G. G. Paulus, H. Walther, R. Kopold, W. Becker, D. B. Milošević, A. Sanpera, and M. Lewenstein, Science **292**, 902 (2001).

[45] L. D. Landau and E. M. Lifshitz, *Course of Theoretical Physics: Quantum Theory*, 3rd ed. (Butterworth-Heinemann, Oxford, 2005), Vol. 3, Sec. 50.

[46] Thomas Brabec, Misha Yu. Ivanov, and Paul B. Corkum, Phys. Rev. A **54**, R2551 (1996).

[47] D. Bauer and P. Koval, Comput. Phys. Commun. **174**, 396 (2006); see, also, www.qprop.de.